




## Article

# Ordered Mesoporous Silica Prepared in Different Solvent Conditions: Application for Cu(II) and Pb(II) Adsorption

Ana-Maria Putz <sup>1</sup>, Oleksandr I. Ivankov <sup>2</sup>, Alexander I. Kuklin <sup>2</sup>, Vasyl Ryukhtin <sup>3</sup>, Cătălin Ianăși <sup>1</sup>, Mihaela Ciopec <sup>4</sup>, Adina Negrea <sup>4</sup>, László Trif <sup>5</sup>, Zsolt Endre Horváth <sup>6</sup> and László Almásy <sup>7,\*</sup>

<sup>1</sup> “Coriolan Drăgulescu” Institute of Chemistry, Bv. Mihai Viteazul, No. 24, 300223 Timisoara, Romania; putzanamaria@acad-icht.tm.edu.ro (A.-M.P.); cianasic@yahoo.com (C.I.)

<sup>2</sup> Frank Laboratory of Neutron Physics, Joint Institute for Nuclear Research, Joliot-Curie 6, 141980 Dubna, Russia; ivankov@jinr.ru (O.I.I.); kuklin@jinr.ru (A.I.K.)

<sup>3</sup> Nuclear Physics Institute, ASCR, Husinec—Řež 130, 250 68 Řež, Czech Republic; ryukhtin@ujf.cas.cz

<sup>4</sup> Faculty of Industrial Chemistry and Environmental Engineering, Politehnica University Timișoara, 6th Vasile Pârvan Bvd., 300223 Timisoara, Romania; mihaela.ciopec@upt.ro (M.C.); adina.negrea@chim.upt.ro (A.N.)

<sup>5</sup> Institute of Materials and Environmental Chemistry, Research Centre for Natural Sciences, Magyar Tudósok Körútja 2, 1117 Budapest, Hungary; trif.laszlo@ttk.hu

<sup>6</sup> Institute for Technical Physics and Material Science, Centre for Energy Research, Konkoly-Thege Miklós út 29-33, 1121 Budapest, Hungary; horvath.zsolt.endre@ek-cer.hu

<sup>7</sup> Institute for Energy Security and Environmental Safety, Centre for Energy Research, Konkoly-Thege Miklós út 29-33, 1121 Budapest, Hungary

\* Correspondence: almasy.laszlo@ek-cer.hu



**Citation:** Putz, A.-M.; Ivankov, O.I.; Kuklin, A.I.; Ryukhtin, V.; Ianăși, C.; Ciopec, M.; Negrea, A.; Trif, L.; Horváth, Z.E.; Almásy, L. Ordered Mesoporous Silica Prepared in Different Solvent Conditions: Application for Cu(II) and Pb(II) Adsorption. *Gels* **2022**, *8*, 443. <https://doi.org/10.3390/gels8070443>

Academic Editors: Francesco Caridi, Giuseppe Paladini and Andrea Fiorati

Received: 23 June 2022

Accepted: 13 July 2022

Published: 15 July 2022

**Publisher’s Note:** MDPI stays neutral with regard to jurisdictional claims in published maps and institutional affiliations.



**Copyright:** © 2022 by the authors. Licensee MDPI, Basel, Switzerland. This article is an open access article distributed under the terms and conditions of the Creative Commons Attribution (CC BY) license (<https://creativecommons.org/licenses/by/4.0/>).

**Abstract:** In this work, the synthesis of ordered mesoporous silica of MCM-41 type was investigated aimed at improving its morphology by varying the synthesis conditions in a one-pot process, employing different temperatures and solvent conditions. 2-methoxyethanol was used as co-solvent to ethanol. The co-solvent ratio and the synthesis temperature were varied. The pore morphology of the materials was characterized by nitrogen porosimetry and small angle neutron scattering (SANS), and the particle morphology by transmission electron microscopy (TEM) and ultra-small angle neutron scattering (USANS). The thermal behavior was investigated by simultaneous thermogravimetry-differential scanning calorimetry (TG-DSC) measurements. The SANS and N<sub>2</sub> sorption results demonstrated that a well-ordered mesoporous structure was obtained at all conditions in the synthesis at room temperature. Addition of methoxyethanol led to an increase of the pore wall thickness. Simultaneously, an increase of methoxyethanol content led to lowering of the mean particle size from 300 to 230 nm, according to the ultra-small angle scattering data. The ordered porosity and high specific surfaces make these materials suitable for applications such as adsorbents in environmental remediation. Batch adsorption measurements of metal ion removal from aqueous solutions of Cu(II) and Pb(II) showed that the materials exhibit dominantly monolayer surface adsorption characteristics. The adsorption capacities were 9.7 mg/g for Cu(II) and 18.8 mg/g for Pb(II) at pH 5, making these materials competitive in performance to various composite materials.

**Keywords:** MCM-41; SANS; USANS; SAXS; Stöber method; 2-methoxyethanol; Langmuir isotherm

## 1. Introduction

Numerous research has dealt with the problem of obtaining suitable adsorbents in order to remove the hazardous pollutants. Adsorption technology is the most promising and frequently used approach due to its simplicity, high efficiency and low cost [1]. Various kinds of sorbent materials, both natural and synthetic, have been used to remove heavy metal ions from aqueous solution. Low cost industrial and agricultural by-products and waste materials usually have low adsorption efficiency because of their low pore volumes and poor pore structure [2,3]. Novel nanomaterials, including carbon-based nanomaterials,

metal-oxide based nanomaterials, nanoparticles and various nanocomposites have been systematically applied for the removal of heavy metal ions from wastewater [4–11].

Due to their simplicity and abundance, silica and silica-based sorbents obtained from natural bio or waste sources represent an emerging approach in applications for removal of industrial pollution [12–17].

Synthetic silica based mesoporous materials, in spite of their higher costs, have also received wide attention and have been widely used for the adsorption of heavy metal ions due to their exceptionally large specific surface area, regular pore structure and suitability for surface modifications [18–21].

Silica materials with ordered porosity and open pore network, such as MCM-41 and SBA-15, are especially suitable for capturing species from aqueous solutions. In the classical synthesis of MCM-41-type materials, the silica precursors and the surfactant molecules used for pore templates are dissolved in water-ethanol mixtures. Full or partial replacement of ethanol with another co-solvent can modify the reaction speed of the sol-gel process, and change the morphology of the resulting silica gel [22,23]. The more hydrophobic 2-methoxyethanol has been used previously as a co-solvent in sol-gel synthesis of uniform spherical silica nanoparticles [24]. Hydrophobic organic co-solvents can affect the pore size by mingling with the surfactant molecules and acting as spacers inside the micelles [25,26]. For example, it was proven that ethoxyethanol acts not only as solvent but also as co-surfactant, controlling the morphology and pore structure. In alkali-catalyzed reactions, the co-surfactants promote the water solubility of the silica precursor tetraethoxysilane (TEOS), facilitating the hydrolysis reactions [27,28]. In previous works, 2-methoxyethanol was used as a protic polar solvent playing different specific roles: as solvent and complexing agent in the synthesis of mixed silica–titania [29], or as a solvent as well as a stabilizer of alkoxide in the hydrolysis-precipitation reaction, allowing one to control the reactivity of the precursors by adjustment of the quantity of 2-methoxyethanol [30].

In the present study, we applied a simple sol-gel synthesis procedure to obtain sorbent materials suitable, among other applications, for water pollutant removal. Two series of ordered mesoporous silica were synthesized, one at room temperature and the other one at 50 °C, and different amounts of 2-methoxyethanol were used in the range of 0:1 to 3:1 relative to the ethanol content. Cetyltrimethylammonium bromide (CTAB) was used as a pore forming agent. The influence of the mixed solvent composition and synthesis temperature on the particle morphology and the pore network was studied by small angle neutron scattering and nitrogen porosimetry.

The applicability of the obtained materials as adsorbents for heavy metals ions from water was studied with the example of Pb(II) and Cu(II).

## 2. Results and Discussion

### 2.1. FT-IR Analysis

All samples (xerogels and thermally treated materials) show the specific vibration bands for the silica skeleton at 1055–1085  $\text{cm}^{-1}$ , 785–805  $\text{cm}^{-1}$  and 450–455  $\text{cm}^{-1}$  (Figure 1). This is assigned to the asymmetric stretching [31,32], symmetric stretching [33,34] and bending rocking mode vibration of the Si-O-Si network [32], respectively. For all calcined samples, the asymmetric stretching vibration bands are shifted to higher values by approximately 20–30  $\text{cm}^{-1}$ . This effect is related to the densification of the silica network [34]. The 1640  $\text{cm}^{-1}$  vibration band belongs to molecular water [35]. The presence of the silanol groups was confirmed by the presence of the band centered about 960  $\text{cm}^{-1}$ , which is associated with the stretching mode of the Si-OH groups [35]. The broad band centered at around 3440–3405  $\text{cm}^{-1}$  corresponds to the O-H stretching bands of hydrogen-bonded water molecules (H-O-H $\cdots$ H) and the Si-O-H stretching of surface silanols hydrogen-bonded to water (-SiOH $\cdots$ H<sub>2</sub>O) [33]. They become more intense after calcination due to the increased hygroscopicity of the calcined samples, because the removal of the surfactant molecules allows some water to enter the pores [36].

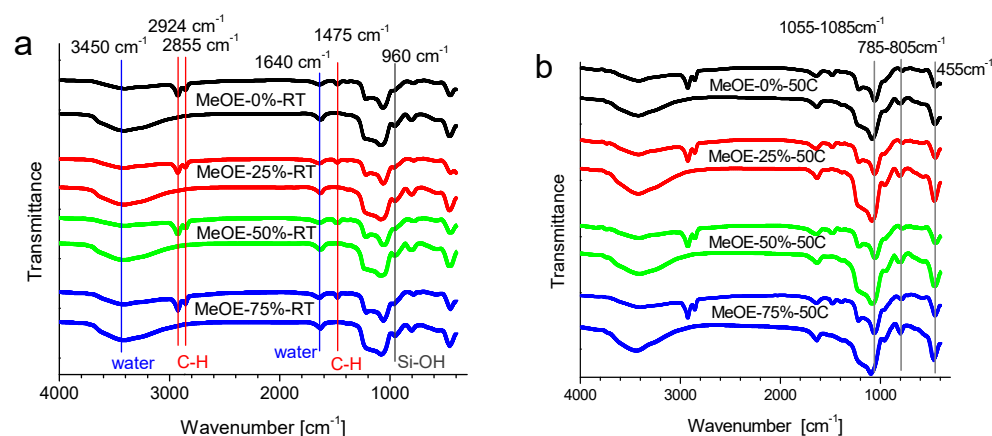


**Figure 1.** FT-IR spectra of mesoporous silica synthesized at room temperature (a) and at 50 °C (b), before and after calcination. Vertical lines in panel (a) show the characteristic bands of CTAB that disappear after thermal treatment (red); the vibrations related to water (blue) and Si-OH vibrations (dark grey). The vertical lines in panel (b) show the characteristic bands of the silica network.

Another group of characteristic vibrations is due to surfactant molecules. In the non-calcined samples, the bands at 2924 and 2855  $\text{cm}^{-1}$  are the asymmetric and symmetric stretching vibrations of the alkyl chain, respectively, and the band around 1475  $\text{cm}^{-1}$ , is the bending vibration of the C-H groups [35]. These bands completely disappear after calcination for all samples (Figure 1).

## 2.2. Thermal Analysis

Thermogravimetric and scanning calorimetry analyses in synthetic air were performed on the RT series of xerogels not subjected to calcination. The weight loss curves for the four samples are shown in Figure 2a. On the DTG curves (Figure 2b), five distinct weight loss regions can be identified, from which the second and the third steps are overlapped. In the first temperature range between 25 and 150 °C, physisorbed water evaporates, which is accompanied by a small and broad endotherm (Figure 2c). Between 150 and 350 °C, the surfactant decomposes and burns out. The two overlapped peaks on the DTG curve can be attributed to the separate oxidation and decomposition of the tetramethyl ammonium headgroups and the long alkyl chains of the CTAB. The oxidative burning of the organic matter is accompanied by a sharp and large exothermic signal on the heat flow curves around 340 °C. Between 400 and 700 °C, the small weight loss, accompanied by a small and broad exotherm, can be attributed to the complete oxidation and elimination of the decomposed organic compounds from the pores.

The spike-like exothermic peaks in the DSC curves at around 720–740 °C indicate phase transformations in the silica matrix.

In their thermal behavior, no systematic differences between the four samples were observed, which can be explained by the small differences in the morphology, and indicate that not much of methoxyethanol remained entrapped in the pores after the washing procedure during synthesis. The total weight loss of about 50% in the whole temperature range corresponds to the typical content of CTAB surfactant in the MCM-41 type materials [36].

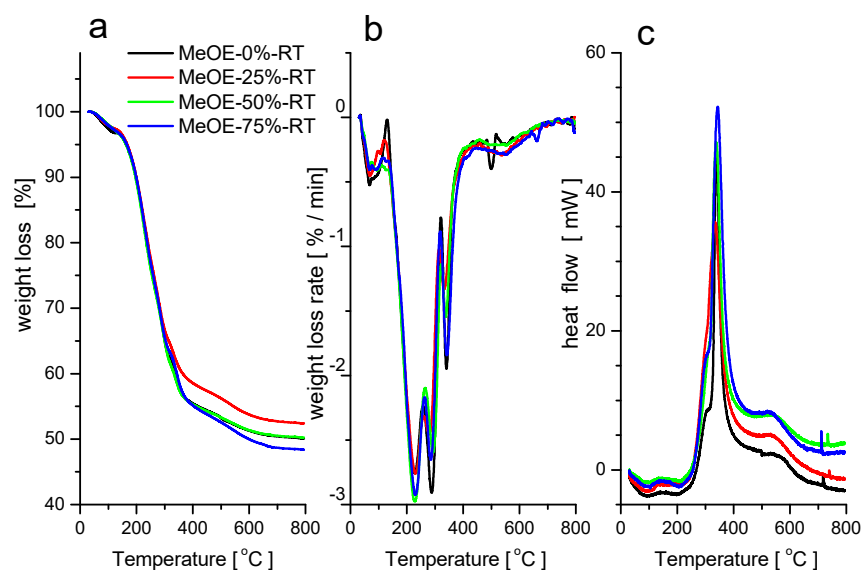


**Figure 2.** TG (a), DTG (b) and DSC (c) curves for samples prepared at room temperature.

### 2.3. Nitrogen Porosimetry

The nitrogen physisorption isotherms for all materials are shown in Figure 3. The materials present type IVb isotherm according to IUPAC classification. Type IVb is specific for mesoporous materials having conical or cylindrical pores, closed at one end [37,38]. The narrow hysteresis in the interval 0.2–0.4  $P/P_0$  suggests the presence of some wide pores that could have more access to the external surface [38].

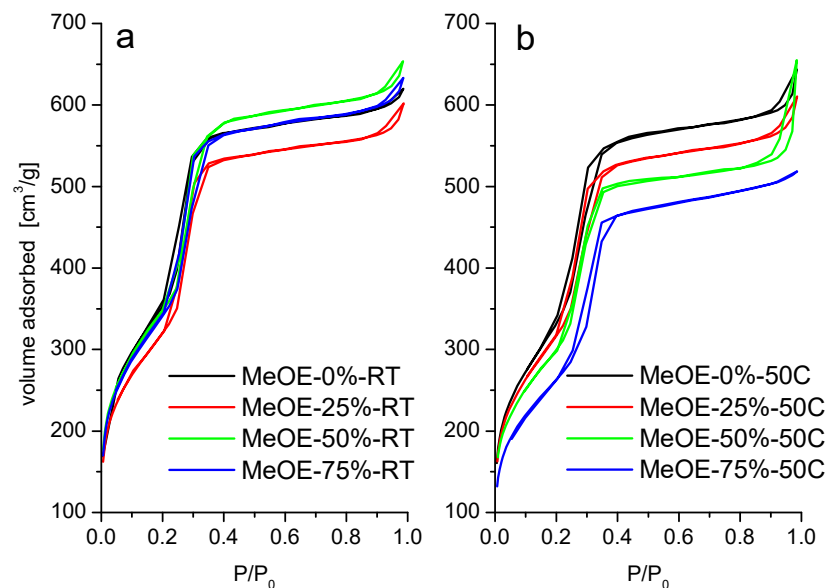


**Figure 3.**  $N_2$  adsorption-desorption isotherms of calcined samples prepared at room temperature (a) and at 50 °C (b).

The pore size distribution (Figure 4) is narrow and centered around 3.5 nm for all samples. The BJH mean pore size shows a small increase from 3.0 to 3.3 nm, with the increase of methoxyethanol concentration in the solvent. The total pore volume does not change appreciably, except for the samples prepared with the highest methoxyethanol content at 50 °C when it drops by about 40%. This is related to the partial collapse of the pores, as shown later by the SANS results.

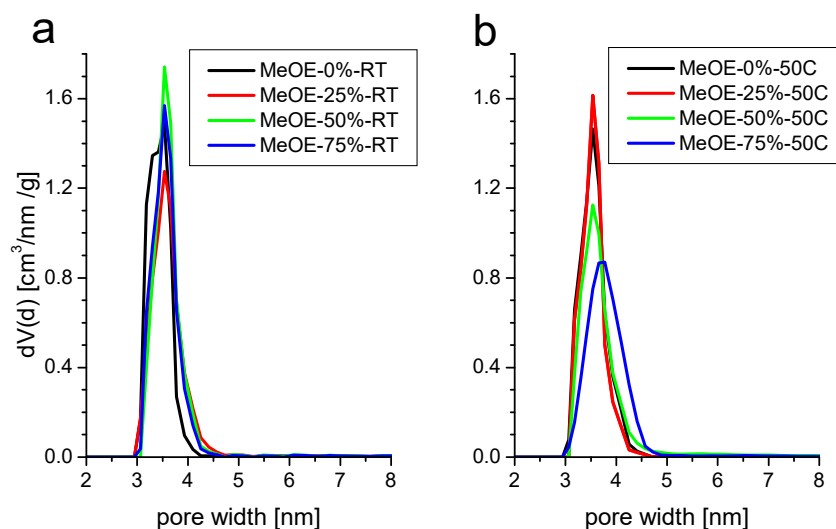


**Figure 4.** Pore size distribution of samples synthesized at room temperature (a) and at 50 °C (b).

The different texture of the materials was also observed in the surface fractal dimensions evaluated by Frenkel-Halsey-Hill (FHH) method [39]. The FHH model is used to determine the fractal geometry and calculate surface structure and irregularities. Value of  $D_f$  2 indicates smooth surface and 3 is characteristic for a porous surface [39]. The FHH data (Table 1) indicate that using methoxyethanol as co-solvent a smoother surface is obtained compared to the materials prepared only with ethanol.

**Table 1.** Textural parameters of the calcined MCM-41 samples.

Sample	BET Surface Area ( $\text{m}^2/\text{g}$ )	BET Constant	Pore Width (DFT) (nm)	Mean Pore Size (BJH) (nm)	Mean Pore Size (BJH) (nm)	Total Pore Volume ( $\text{cm}^3/\text{g}$ )	$D_f$ (Adsorpt.)	$D_f$ (Desorpt.)
MeOE-0%-RT	1793	10	3.53	3.30	3.07	0.961	2.846	2.876
MeOE-25%-RT	1540	12	3.53	3.39	3.06	0.933	2.762	2.830
MeOE-50%-RT	1620	13	3.53	3.41	3.34	1.013	2.761	2.828
MeOE-75%-RT	1547	15	3.53	3.41	3.31	0.981	2.764	2.839
MeOE-0%-50C	1568	13	3.53	3.39	3.07	0.998	2.750	2.864
MeOE-25%-50C	1446	15	3.53	3.40	3.04	0.946	2.757	2.865
MeOE-50%-50C	1428	12	3.53	3.06	3.06	1.016	2.750	2.864
MeOE-75%-50C	1074	24	3.78	3.39	3.31	0.804	2.738	2.822

Materials synthesized at 50 °C present almost the same characteristics. The isotherms are of type IVb with a narrow hysteresis (Figure 3b). The surface area decreases with increasing methoxyethanol content. For this series, the pore size distribution is somewhat broader, especially for the highest methoxyethanol content (Figure 4b).

All textural parameters for surface area, total pore volume and mean pore diameter are shown in Table 1. The highest BET surface area of  $1793 \text{ m}^2/\text{g}$  was obtained for sample synthesized at room temperature, and all samples had surface areas above  $1000 \text{ m}^2/\text{g}$ . With increasing 2-methoxyethanol content in the solvent mixture, the surface area decreased in both series. The changes in the surface area and roughness can be related to the lowering of the speed of hydrolysis and condensation with addition of methoxyethanol having hydrophobic methyl and methylene groups.

#### 2.4. Electron Microscopy

TEM micrographs of the two investigated samples showed spherical and slightly elongated particles with sizes of 200–400 nm, typical for silica obtained in the Stöber synthesis process (Figure 5). Well-developed parallel channels with hexagonal ordering



confirmed the structure of the MCM-41 materials. There were no noticeable differences between the samples MeOE-0%-RT and MeOE-75%-RT, in the selected areas of the TEM images.

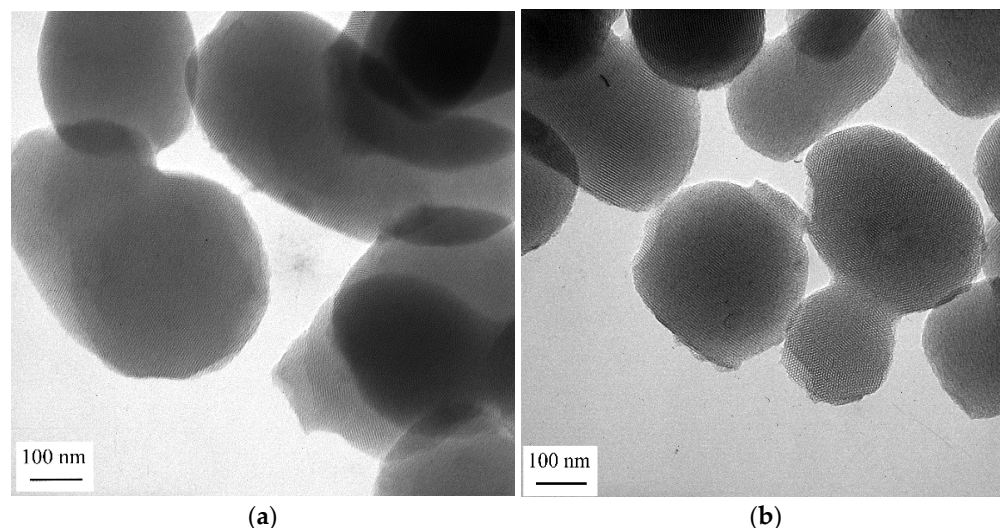


**Figure 5.** Characteristic TEM images of mesoporous silica prepared at room temperature without 2-methoxyethanol (a) and in solvent with 3:1 methoxyethanol/ethanol ratio (b).

### 2.5. Small Angle Neutron Scattering

SANS curves for the two series taken on spectrometer YuMO are shown in Figure 6a,b. All samples show the typical organized structure of MCM-41 type, exhibiting the (100), (110), (200) reflections of the hexagonal pore structure [40–42]. The (110) and (200) peaks are smeared because of the moderate instrumental resolution related to the relaxed collimation and finite detector ring size, characteristic for small-angle neutron instruments. The sample prepared at 50 °C using 75% methoxyethanol is disordered (Figure 6b) and the diffraction peaks are nearly invisible. No well-ordered structure formed in the synthesis at these conditions, and the xerogel filled with CTAB was weaker and the pore structure was destroyed during calcination. Another characteristic difference between the samples prepared at the two temperatures is the width of the first diffraction peak, which is broader for the 50 °C synthesis, indicating a weaker long-range ordering. For samples prepared at room temperature, a significant difference was seen in the (100) peak position, between the material prepared in pure ethanol solvent, and the three samples prepared in mixed solvents. The peak position for MeOE-0%-RT sample was smaller by 3%, showing larger inter-pore distance, which indicates a larger wall thickness (Figure 7). This effect can be related to the slower condensation rate of the silica the presence of 2-methoxyethanol as cosolvent.

Measurements of the RT sample series in the very low  $q$  range, performed on the MAUD instrument, allowed us to assess the overall dimensions of the nanoparticles. The scattering curves measured with the medium and low-resolution instrument settings (solid and open symbols) are shown in Figure 8. The scattering data were fitted to a model of polydisperse spherical particles with log-normal size distribution. The resulting mean diameters were in the range of 200–300 nm, which is typical for Stöber synthesis. Interestingly, a well distinguished monotonous change of the particle size in the function of methoxyethanol content was observed: the larger (300 nm) particles were obtained using pure ethanol-water solvent mixture, and the gradual replacement of ethanol by 2-methoxyethanol resulted in smaller (230 nm) particles.

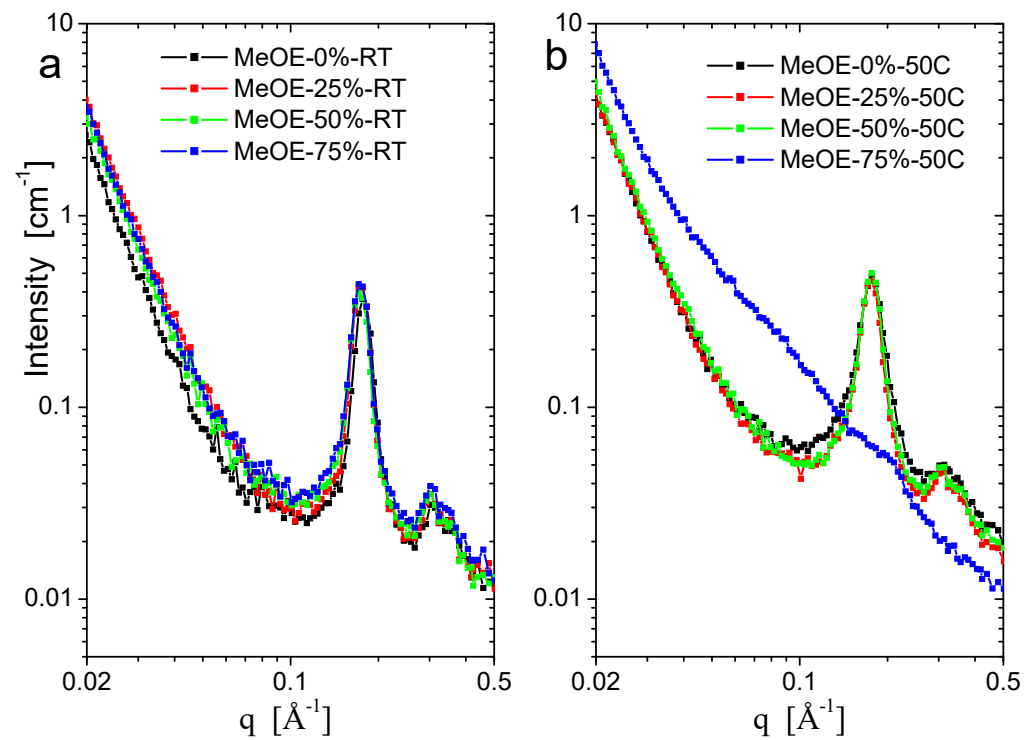


**Figure 6.** SANS scattering curves of samples prepared at room temperature (a) and at 50 °C (b).

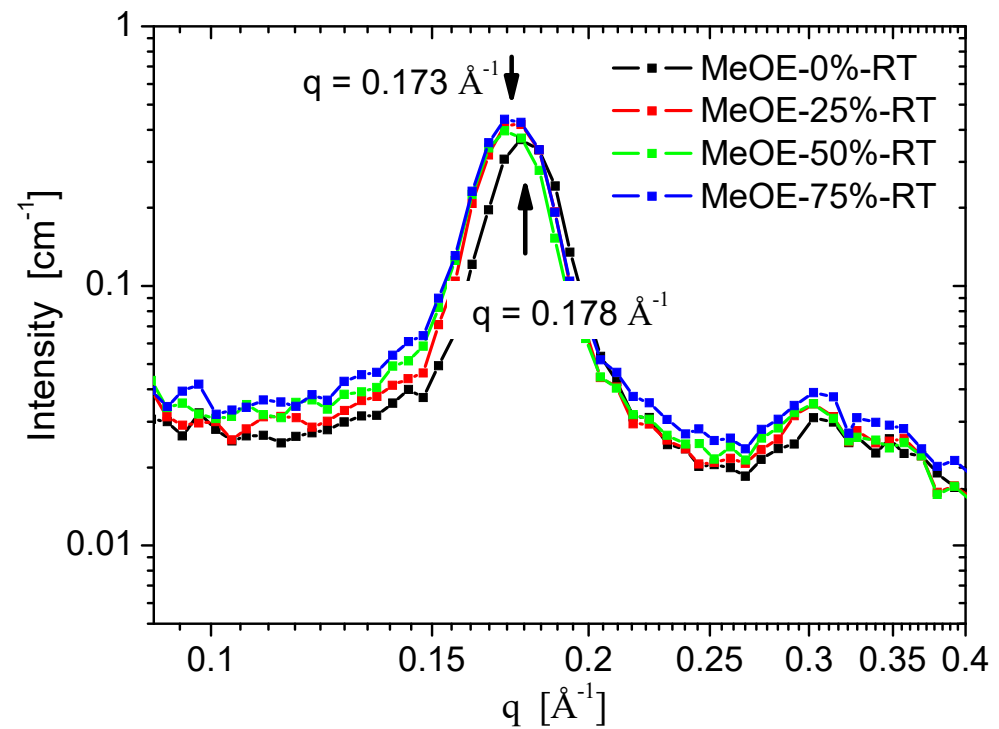


**Figure 7.** Variation of the first diffraction peak position with the content of 2-methoxyethanol in the solvent mixture.

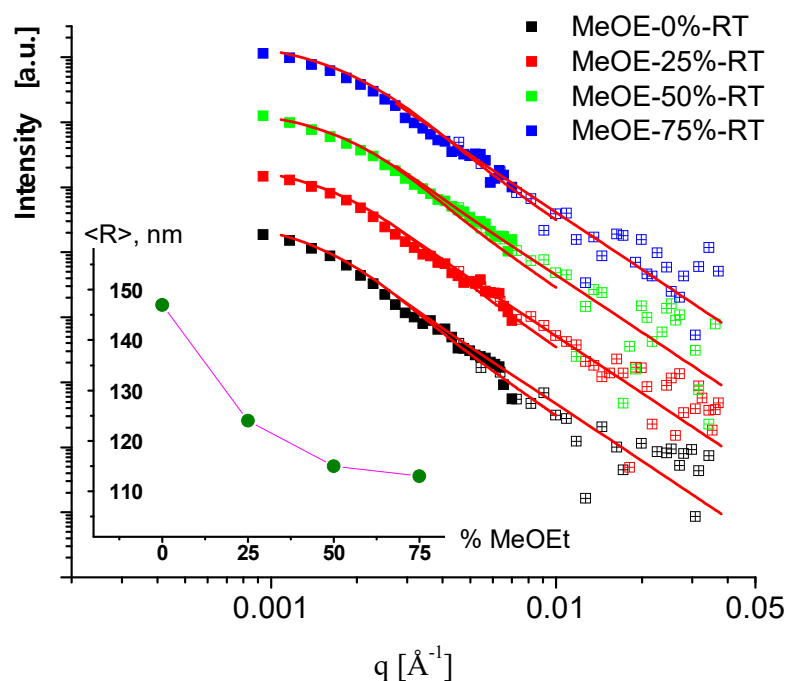


**Figure 8.** USANS scattering curves of samples prepared at room temperature. Symbols are the measured data, and red solid lines are the fitted model of polydisperse spheres. Data are shifted vertically. In the inset, the mean radius of the particles is shown in the function of 2-methoxyethanol content in the sol.

### 2.6. Metal Ion Adsorption

Adsorption isotherms are powerful tools for the analysis of adsorption processes. They establish the relationship between the equilibrium concentration and the amount adsorbed by unit mass of the adsorbent at a constant temperature. Adsorption studies were performed at pH 5 because it was shown previously for these kind of materials that the maximum adsorption capacities for  $\text{Cu}^{2+}$  and  $\text{Pb}^{2+}$  were observed at pH 5.0 [19]. First, all eight samples were tested for adsorption of  $\text{Cu}(\text{II})$  and  $\text{Pb}(\text{II})$ , and then the material with the best adsorption capacity for  $\text{Cu}(\text{II})$ , (sample MeOE-75%-RT), and the material with the best adsorption capacity for  $\text{Pb}(\text{II})$ , (sample MeOE-0%-RT) were selected for construction of the adsorption isotherms. The equilibrium time for adsorption was determined varying the time in the range 15–180 min for a  $\text{Me}(\text{II})$  ions concentration of 10 mg/L. After 2 h, the adsorption capacity has a constant value. Two hours of contact time was used in constructing the adsorption isotherms.

The adsorption capacity  $q$  (mg/g), was determined using the following equation:

$$q = (C_0 - C_f) \frac{V}{m} \quad (1)$$

where  $C_0$  and  $C_f$  are the initial and final concentrations of metallic ions in solution in the beginning and the end of the adsorption test, respectively (mg/L),  $V$  is the volume of the solution (L) and  $m$  is the mass of the adsorbent (g).

The adsorption isotherms of  $\text{Me}(\text{II})$  ions are presented in Figure 9. The Langmuir, Freundlich and Sips isotherms were used to model experimental data in order to establish the adsorption mechanism and the maximum adsorption capacity [43,44].



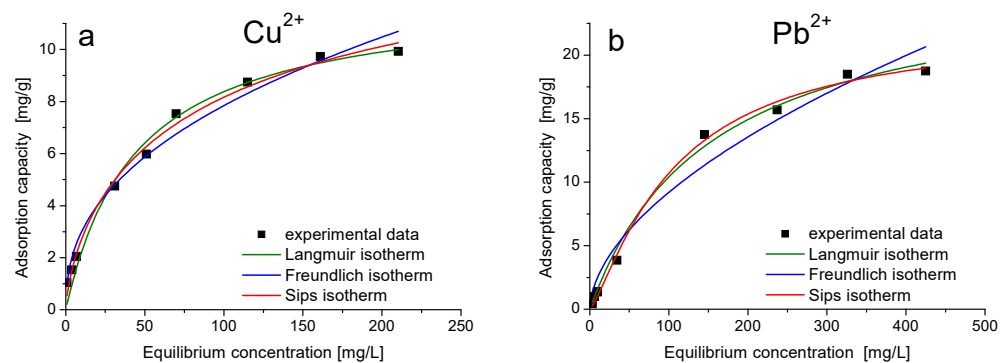


Figure 9. Adsorption isotherms of (a) Cu(II) on MeOE-75%-RT and (b) Pb(II) on MeOE-0%-RT.

The non-linear form of the Langmuir isotherm equation [45] can be expressed as follows:

$$q_e = \frac{q_L K_L C_f}{1 + K_L C_f} \tag{2}$$

where  $q_e$  is the equilibrium adsorption capacity (mg/g);  $C_f$  is the equilibrium ion concentration in solution (mg/L);  $q_L$  is the Langmuir maximum adsorption capacity (mg/g) and  $K_L$  is the Langmuir constant.

The Freundlich isotherm is applicable to heterogeneous adsorption surfaces. The non-linear form of the Freundlich isotherm equation [46] is:

$$q_e = K_F C_f^{1/n_f} \tag{3}$$

where  $K_F$  and  $n_f$  are the characteristic constants related to the adsorption capacity of the adsorbent and the intensity of adsorption.

The Sips or Langmuir-Freundlich isotherm (Equation (4)) derives from the Freundlich and Langmuir models. It reduces to a Freundlich isotherm at low adsorbate concentrations. At high adsorbate concentrations, the Sips isotherm has the characteristics of the Langmuir isotherm and therefore can be used to calculate the monolayer adsorption capacity [47].

$$q_e = \frac{q_S K_S C_e^{1/n_S}}{1 + K_S C_e^{1/n_S}} \tag{4}$$

where  $K_S$  (mg/g) is a constant related to the adsorption capacity of the adsorbent and  $n_S$  is the heterogeneity factor. As the surface heterogeneity is higher, the deviation of  $1/n_S$  value from 1 will be higher. The parameters of Langmuir, Freundlich and Sips isotherms determined using non-linear regression are listed in Table 2.

Table 2. Langmuir, Freundlich and Sips isotherm parameters for Cu(II) ions adsorption on sample MeOE-75%-RT and Pb(II) on MeOE-0%-RT.

Adsorbent /Metal Ion	$q_{m,exp}$ (mg/g)	Langmuir Isotherm			Freundlich Isotherm			Sips Isotherm			
		$q_L$ (mg/g)	$K_L$	$R^2$	$K_F$ (mg/g)	$1/n_F$	$R^2$	$K_S$	$q_S$ (mg/g)	$1/n_S$	$R^2$
MeOE-75%-RT /Cu <sup>2+</sup>	9.7	7.3	0.022	0.988	1.14	0.41	0.978	0.0026	10.2	0.3	0.990
MeOE-0%-RT /Pb <sup>2+</sup>	18.8	26.3	0.065	0.993	0.7	0.5	0.963	0.0061	22.2	0.6	0.995

The adsorption capacity increased with increasing equilibrium concentration of Me(II) ions. The experimental isotherms show the approach of the adsorption capacity to constant value and, correspondingly, the large deviation of the fitted Freundlich model curves

from the data. The maximum adsorption capacity of Cu(II) on sample MeOE-75%-RT for an initial Cu(II) concentration of 250 mg/L is  $q_{m,exp} = 9.7$  mg/g, and the maximum adsorption capacity of Pb(II) on sample MeOE-0%-RT is  $q_{m,exp} = 18.8$  mg/g for an initial Pb(II) concentration of 500 mg/L.

For both materials, the adsorption is better described by the Sips isotherm. The maximum adsorption capacity obtained by modelling the experimental data with Sips isotherm is  $q_s = 10.2$  mg Cu(II)/g sorbent, a value very close to the experimental value  $q_{m,exp} = 9.7$  mg Cu(II)/g sorbent for sample MeOE-75%-RT and  $q_s = 22.2$  mg/g, a value very close to the experimental value  $q_{m,exp} = 18.8$  mg Pb(II)/g for sample MeOE-0%-RT at the highest salt concentration. Parameter  $1/n$  in the Sips model is a measure of the adsorption intensity or surface heterogeneity. For  $1/n = 1$ , the partition between the two phases is independent of the concentration. The situation  $1/n < 1$  is the most commonly encountered and corresponds to Langmuir isotherm, while  $1/n > 1$  indicates cooperative adsorption involving strong interactions between the molecules of the adsorbate [48,49]. The value of the heterogeneity factor  $1/n_s$  was obtained as 0.3 for sample MeOE-75%-RT and 0.6 for sample MeOE-0%-RT, indicating that the heterogeneity of the surface was very low. This suggests that the adsorption mechanism approaches the monolayer adsorption and the adsorption of Me(II) ions onto adsorbent materials was a favourable process.

The maximum adsorption capacities of these materials were compared to some other adsorbents from recent literature (Table 3). Concerning the Pb(II) adsorption, the obtained value of 18.8 mg/g proved that our mesoporous silica has better adsorption properties compared with kaolin, activated carbon and zeolite, but worse than the functionalized mesoporous silica and the composite materials of iron oxide nanoparticles with functionalized porous silica or cellulose (Table 3). Concerning the Cu(II) adsorption, the obtained value of 9.7 mg/g for the adsorption capacity is higher than that of zeolites, similar to magnetite nanoparticles, but worse than the adsorption capacities of other metal oxide nanoparticles or mesoporous silica having different functional groups. Therefore, the functionalization of mesoporous silica materials is necessary to improve their adsorption capacity for metal ions removal. On the other hand, the ease of preparation and low cost of the nonfunctionalized mesoporous silica may compensate for their lower performance in certain applications.

**Table 3.** Comparison of the Me(II) adsorption capacity of the prepared mesoporous silica samples to other adsorbent materials.

Sorbent	Metal Ion	Adsorption Capacity (mg/g)	Reference
Kaolin		4.5	[50]
activated carbon		6.7	[50]
magnetic chlorapatite nanoparticles		238	[51]
zeolite		9.9	[52]
thiol functionalized iron-oxide loaded FDU-12 mesoporous silica		287	[53]
Fe <sub>3</sub> O <sub>4</sub> @carboxymethyl-cellulose		152	[54]
Fe <sub>3</sub> O <sub>4</sub> @SiO <sub>2</sub> @DMSA		50.5	[55]
Fe <sub>3</sub> O <sub>4</sub> @SiO <sub>2</sub> @TSD		417	[56]
Fe <sub>3</sub> O <sub>4</sub> @SiO <sub>2</sub> -NH <sub>2</sub>		76.6	[57]
pretreated <i>Aspergillus niger</i>		32.6	[58]
maghemite nanoparticle		68.9	[59]
magnetite nanoparticles		37.3	[60]
TiO <sub>2</sub> nanoparticles	Pb(II)	21.7	[61]
Al <sub>2</sub> O <sub>3</sub> nanoparticles		41.2	[61]
MgO nanoparticles		148	[61]
Chitosan/graphene oxide		461	[62]
silica@ketoenol-pyrazole		41.8	[63]
ZnCl <sub>2</sub> -MCM-41		479	[64]

Table 3. Cont.

Sorbent	Metal Ion	Adsorption Capacity (mg/g)	Reference
EDTA/SBA-15		273	[65]
waste silica coated by iron oxide		8.2	[66]
silica-magnetite composite		14.9	[67]
citrate coated SPION		58.9	[68]
gelatin-siloxane hybrid		3.75	[11]
chitosane-alginate hydrogel		85	[9]
thiol functionalized silica/magnetite		0.8	[69]
magnetic nano-zeolite		476.1	[70]
nano-silica made of <i>Saccharum officinarum</i>		148	[71]
<b>Calcined MCM-41</b>		18.8	<b>Present paper</b>
zeolite		8.5	[52]
Fe <sub>3</sub> O <sub>4</sub> @SiO <sub>2</sub> -NH		29.9	[57]
pretreated <i>Aspergillus niger</i>		28.7	[58]
maghemite nanoparticle		34.0	[59]
magnetite nanoparticles		10.8	[60]
TiO <sub>2</sub> nanoparticles		50.2	[61]
Al <sub>2</sub> O <sub>3</sub> nanoparticles		47.9	[61]
MgO nanoparticles		149.1	[61]
Chitosan/graphene oxide		423.8	[62]
silica@ketoenol-pyrazole	<b>Cu(II)</b>	76.9	[63]
waste silica coated by iron oxide		3.4	[66]
magnetic nano-zeolite		59.9	[70]
steel slag/CNT composite		132.8	[72]
bifunctional silica nanospheres		139.8	[73]
nanosilica/nanopolyaniline		108	[74]
nanosilica/crosslinked nanopolyaniline		105	[74]
gelatin-siloxane hybrid		1.76	[11]
core-shell magnetite-silica NP		41	[75]
<b>Calcined MCM-41</b>		9.7	<b>Present paper</b>

### 3. Conclusions

In this paper we studied morphology evolution of ordered mesoporous silica nanoparticles of MCM-41 type, prepared at different solvent conditions using 2-methoxyethanol as a co-solvent and CTAB as a pore forming molecule, by conventional pin-hole and slit-smear ultra-small-angle neutron scattering. The use of mixed solvent resulted in larger wall thickness and interpore distance, and the hexagonal mesoporous structure was maintained up to 75/25 methoxyethanol/ethanol ratio. This effect can be related to the slower condensation rate of the silica network in the presence of 2-methoxyethanol as cosolvent. These structural changes were accompanied by a 10% decrease of the surface area, as measured by nitrogen sorption. A weaker long-range ordering was obtained for the samples synthesized at elevated temperature of 50 °C. These textural and structural observations show that varying the solvent conditions and temperature allows one to tune and optimize the porosity and intrapore surface of the materials, which is of primary importance for their applications as sorbent materials. In future work the effect of other synthesis conditions should be explored aiming to achieve the highest porosity, high specific surface and surface quality modification by functional groups, for achieving efficient binding of metal and organic pollutants.

Selected samples were tested for adsorption of metal pollutants from aqueous phase. The adsorption equilibrium data of Pb(II) and Cu(II) followed the Sips and the Langmuir isotherms, while the Freundlich model did not fit the experimental data. The modeling showed that the heterogeneity of the adsorbent materials surface was very low, suggesting that the adsorption mechanism approached monolayer adsorption. Comparison of the adsorption performance of the prepared materials to various adsorbents from the literature

revealed that the adsorption capacity of the present mesoporous silica is comparable to some simple materials, but lower than many of the much more expensive composite materials.

This study showed that while the modification of the structure, overall dimension and pore size can be tuned easily within narrow limits by changing the solvent composition, the resulting effect on the adsorption performance is not particularly strong within the investigated synthesis conditions. This is attributed to the relatively small change of the pore size and internal surface by the simple solvent variation method. Replacement of the traditional CTAB with longer or shorter alkyl chain surfactants can efficiently vary the porosity within a certain range. Furthermore, using more eco-friendly biosurfactants may be beneficial in long term, after resolving the most prohibitive factors such as their high costs and low productivity [76].

## 4. Materials and Methods

### 4.1. Sample Preparation

The following chemicals were used: tetraethoxysilane (TEOS), (99%, for analysis, Fluka Chemie, Buchs, Switzerland); hexadecyltrimethyl ammonium bromide (CTAB, Sigma-Aldrich, Darmstadt, Germany); ethanol (Chimopar, Bucharest, Romania); 2-methoxyethanol (99%, for analysis, Sigma-Aldrich); ammonia solution 25% (Adra Chim SRL, Bucharest, Romania).

Ordered mesoporous silica materials were prepared by sol-gel synthesis in alkaline conditions, using TEOS as silica precursor and CTAB as pore forming agent, adopting traditional methods [22,77] for using solvent mixtures. As solvent, ethanol and 2-methoxyethanol were used in different proportions. A quantity of 1 g CTAB was added to 192.49 mL of distilled H<sub>2</sub>O under stirring. After the solution turned clear, 68 mL of alcohol was added and then 23.2 mL of aqueous ammonia solution (25%) was added, and the samples were stirred for 30 min. Ethanol was used for the first sample from each series and it was progressively substituted with 2-methoxyethanol for the next three samples in each series. After that, 4 mL of TEOS was poured into the solution slowly under stirring. Stirring continued for 3 h. After about 20 h, the solid product was recovered by filtration and washed several times with distilled water with repeated filtrations until the pH of the washing water approached the pH value of the distilled water. The samples were dried at room temperature until the next day, then further dried for several hours at 90 °C. CTAB was removed by calcination at 550 °C during 6 h, after a heating ramp with 1 °C/min. The sample names and synthesis parameters are shown in Table 4.

**Table 4.** Synopsis of the synthesized samples.

Sample Name	CTAB (g)	TEOS (mL)	Synthesis Temperature	H <sub>2</sub> O (mL)	Ethanol (mL)	2-Methoxyethanol (mL)
MeOET-0%-RT	1	4	r.t.	192.5	68	0
MeOET-25%-RT	1	4	r.t.	192.5	51	17
MeOET-50%-RT	1	4	r.t.	192.5	34	34
MeOET-75%-RT	1	4	r.t.	192.5	17	51
MeOET-0%-50C	1	4	50 °C	192.5	68	0
MeOET-25%-50C	1	4	50 °C	192.5	51	17
MeOET-50%-50C	1	4	50 °C	192.5	34	34
MeOET-75%-50C	1	4	50 °C	192.5	17	51

### 4.2. Characterization Methods

FTIR spectra were taken on KBr pellets with a JASCO-FT/IR-4200 apparatus. Samples after drying (the xerogel samples) as well as after calcination were studied. N<sub>2</sub> physisorption measurements were done at 77 K using a Quantachrome Nova 1200e apparatus. Prior to the analysis the samples were dried and degassed in vacuum at 80 °C for 4 h.

The surface area was determined by the BET (Brunauer–Emmet–Teller) equation in the relative pressure range ( $P/P_0$ ) 0.01–0.25. Pore size distribution was evaluated with BJH (Barrett–Joyner–Halenda) and DFT (Density Functional Theory) methods. Total pore volumes were determined using the relative pressure point closest to 1.

Thermal measurements were performed on a Setaram LabsysEvo (Lyon, France) TG-DSC system, in flowing (90 mL/min) high purity (99.999%) synthetic air (20% O<sub>2</sub> in N<sub>2</sub>) atmosphere. Samples were weighed into 100 µL Al<sub>2</sub>O<sub>3</sub> crucibles (the reference cell was empty) and were heated from 25 °C to 800 °C with a heating rate of 10 °C/min. The obtained data was blank corrected and further processed with the software Calisto Processing, ver. 2.08. The temperature scale and calorimetric sensitivity were calibrated by a multipoint calibration method in which seven different certified reference materials were used to cover the thermal analyzer's entire operating temperature range.

Transmission electron microscopy (TEM) investigation was carried out on a Philips CM20 transmission electron microscope equipped with LaB<sub>6</sub> electron gun operating at 200 kV. The samples for TEM were prepared by drop-drying suspensions on holey carbon foil coated copper grids.

Small-angle neutron scattering measurements were performed on the YuMO time-of-flight instrument operating at the IBR-2 pulsed reactor source in Dubna, Russia [78,79]. The scattered neutrons were detected using the time-of-flight method by a two-detector set-up with ring wire detectors [80]. Measurements were performed on dry powders at room temperature. Corrections for transmission, background and empty aluminium container scattering were performed using SAS software [81].

Ultrasmall-angle neutron scattering measurements were performed on a double-bent crystal instrument MAUD operating at the thermal channel of the LVR15 10 MW research reactor in Řež, Czech Republic [82].

#### 4.3. Metal Ion Adsorption Measurements

For the metallic ion adsorption experiments, 1000 mg/L metallic ion solution in HNO<sub>3</sub> 0.5 mol/L (Merck standard solution) was used. All other metallic ion solutions were prepared from this solution with appropriate dilution. The pH of the sample solutions was pH 5 and was adjusted by using NaOH buffer solutions with the concentration in the 0.05–0.2 M range, measured using a Mettler Toledo Seven Compact S210 pH meter. Distilled water was used in all experiments.

Equilibrium isotherms were constructed using 0.1 g adsorbent materials placed in 25 mL Cu(II) solution at different initial concentrations (5–250 mg/L), and 25 mL Pb(II) solution at different initial concentrations (5–500 mg/L), at room temperature (25 ± 1 °C) and with a stirring time 2 h, using a thermostated shaker bath Julabo SW23, and shaking speed 200 rpm. The equilibrium time for isotherms adsorption was determined varying the time in the range 15–180 min for a Me(II) ions concentration of 10mg/L. After determination of the residual concentration of the metallic ions and the adsorption capacity, it was found that after 2 h the adsorption capacity has a constant value. After stirring, the samples were separated through filtration. The residual concentration of the metallic ions in filtrate was analysed by atomic absorption spectrometry using a Varian SpectraAA 280 Fast Sequential Atomic Absorption Spectrometer with an air-acetylene flame.

**Author Contributions:** Conceptualization, A.-M.P. and L.A.; methodology, A.-M.P., L.T., A.N., M.C. and L.A.; investigation, A.-M.P., C.I., L.T., A.N., M.C., O.I.I., A.I.K., V.R. and Z.E.H.; resources, A.-M.P. and O.I.I.; data curation, A.-M.P., A.N., M.C., L.A. and V.R.; writing—original draft preparation, A.-M.P., A.N., M.C. and L.A.; writing—review and editing, A.-M.P. and L.A. All authors have read and agreed to the published version of the manuscript.

**Funding:** This research received no external funding.

**Data Availability Statement:** Experimental data are available from the authors.

**Acknowledgments:** A.-M.P. and L.A. thank the Inter-Academic Exchange Program between Romanian Academy and the Hungarian Academy of Sciences. A.-M.P. and O.I.I. thank the scientific cooperation program between Romania and Joint Institute for Nuclear Research, Dubna, Russia. USANS measurements were carried out at the CANAM infrastructure of NPI CAS Řež with the use of reactor LVR-15 supported by the project LM2018120. V.R. acknowledges support from the Czech



Academy of Sciences in the frame of the program “Strategie AV21, No. 23”. L.A. is grateful to A. Elbakyan for facilitating access to scientific literature.

**Conflicts of Interest:** The authors declare no conflict of interest. The funders had no role in the design of the study; in the collection, analyses, or interpretation of data; in the writing of the manuscript; or in the decision to publish the results.

## References

1. Yuan, Q.; Li, N.; Chi, Y.; Geng, W.; Yan, W.; Zhao, Y.; Li, X.; Dong, B. Effect of Large Pore Size of Multifunctional Mesoporous Microsphere on Removal of Heavy Metal Ions. *J. Hazard. Mater.* **2013**, *254–255*, 157–165. [[CrossRef](#)] [[PubMed](#)]
2. De Gisi, S.; Lofrano, G.; Grassi, M.; Notarnicola, M. Characteristics and Adsorption Capacities of Low-Cost Sorbents for Wastewater Treatment: A Review. *Sustain. Mater. Technol.* **2016**, *9*, 10–40. [[CrossRef](#)]
3. Beveridge, A.; Pickering, W.F. The Influence of Surfactants on the Adsorption of Heavy Metal Ions by Clays. *Water Res.* **1983**, *17*, 215–225. [[CrossRef](#)]
4. Yang, J.; Hou, B.; Wang, J.; Tian, B.; Bi, J.; Wang, N.; Li, X.; Huang, X. Nanomaterials for the Removal of Heavy Metals from Wastewater. *Nanomaterials* **2019**, *9*, 424. [[CrossRef](#)]
5. Hu, H.; Zhao, D.; Wu, C.; Xie, R. Sulfidized Nanoscale Zerovalent Iron Supported by Oyster Powder for Efficient Removal of Cr (VI): Characterization, Performance, and Mechanisms. *Materials* **2022**, *15*, 3898. [[CrossRef](#)] [[PubMed](#)]
6. Shen, J.; Wang, N.; Wang, Y.G.; Yu, D.; Ouyang, X. Efficient Adsorption of Pb(II) from Aqueous Solutions by Metal Organic Framework (Zn-BDC) Coated Magnetic Montmorillonite. *Polymers* **2018**, *10*, 1383. [[CrossRef](#)] [[PubMed](#)]
7. Herman, P.; Kiss, A.; Fábíán, I.; Kalmár, J.; Nagy, G. In situ remediation efficacy of hybrid aerogel adsorbent in model aquatic culture of *Paramecium caudatum* exposed to Hg(II). *Chemosphere* **2021**, *275*, 130019. [[CrossRef](#)] [[PubMed](#)]
8. Herman, P.; Fábíán, I.; Kalmár, J. Mesoporous Silica–Gelatin Aerogels for the Selective Adsorption of Aqueous Hg(II). *ACS Appl. Nano Mater.* **2020**, *3*, 195. [[CrossRef](#)]
9. Hamza, M.F.; Hamad, N.A.; Hamad, D.M.; Khalafalla, M.S.; Abdel-Rahman, A.A.; Zeid, I.F.; Wei, Y.; Hessien, M.M.; Fouda, A.; Salem, W.M. Synthesis of Eco-Friendly Biopolymer, Alginate-Chitosan Composite to Adsorb the Heavy Metals, Cd(II) and Pb(II) from Contaminated Effluents. *Materials* **2021**, *14*, 2189. [[CrossRef](#)]
10. Zhang, J.; He, H.; Owusu, A.; Henderson, M.J.; Yan, M.; Tian, Q.; Almásy, L. Efficient and selective sorption of uranyl by hydrated Ti<sub>3</sub>C<sub>2</sub>TX-Li agglomerates. *Environ. Nanotechnol. Monit. Manag.* **2021**, *16*, 100528. [[CrossRef](#)]
11. Wojciechowska, P.; Cierpiszewski, R.; Maciejewski, H. Gelatin-Siloxane Hybrid Monoliths as Novel Heavy Metal Adsorbents. *Appl. Sci.* **2022**, *12*, 1258. [[CrossRef](#)]
12. Kaliannan, D.; Palaninaicker, S.; Palanivel, V.; Dhamodaran, K.; Kadirvelu, K.; Kumaran, S. Sol-Gel Mediated Synthesis of Silica Nanoparticle from *Bambusa Vulgaris* Leaves and Its Environmental Applications: Kinetics and Isotherms Studies. *J. Sol-Gel Sci. Technol.* **2019**, *90*, 653–664. [[CrossRef](#)]
13. Li, Y.; Wang, R.; Luo, X.; Chen, Z.; Wang, L.; Zhou, Y.; Liu, W.; Cheng, M.; Zhang, C. Synthesis of Rice Husk-Based MCM-41 for Removal of Aflatoxin B1 from Peanut Oil. *Toxins* **2022**, *14*, 87. [[CrossRef](#)] [[PubMed](#)]
14. Sarti, E.; Chenet, T.; Stevanin, C.; Costa, V.; Cavazzini, A.; Catani, M.; Martucci, A.; Precisvalle, N.; Beltrami, G.; Pasti, L. High-Silica Zeolites as Sorbent Media for Adsorption and Pre-Concentration of Pharmaceuticals in Aqueous Solutions. *Molecules* **2020**, *25*, 3331. [[CrossRef](#)] [[PubMed](#)]
15. Medeiros de Paula, G.; do Nascimento Rocha de Paula, L.; Freire Rodrigues, M.G. Production of MCM-41 and SBA-15 Hybrid Silicas from Industrial Waste. *Silicon* **2022**, *14*, 439–447. [[CrossRef](#)]
16. Razak, N.A.A.; Othman, N.H.; Shayuti, M.S.M.; Jumahat, A.; Sapiai, N.; Lau, W.J. Agricultural and industrial waste-derived mesoporous silica nanoparticles: A review on chemical synthesis route. *J. Env. Chem. Eng.* **2022**, *10*, 107322. [[CrossRef](#)]
17. Miao, C.; Liang, L.; Zhang, F.; Chen, S.; Shang, K.; Jiang, J.; Zhang, Y.; Ouyang, J. Review of the fabrication and application of porous materials from silicon-rich industrial solid waste. *Int. J. Miner. Metall. Mater.* **2022**, *29*, 424–438. [[CrossRef](#)]
18. Wu, S.; Li, F.; Xu, R.; Wei, S.; Li, G. Synthesis of Thiol-Functionalized MCM-41 Mesoporous Silicas and Its Application in Cu(II), Pb(II), Ag(I), and Cr(III) Removal. *J. Nanopart. Res.* **2010**, *12*, 2111–2124. [[CrossRef](#)]
19. Zhu, W.; Wang, J.; Wu, D.; Li, X.; Luo, Y.; Han, C.; Ma, W.; He, S. Investigating the Heavy Metal Adsorption of Mesoporous Silica Materials Prepared by Microwave Synthesis. *Nanoscale Res. Lett.* **2017**, *12*, 323. [[CrossRef](#)]
20. Putz, A.-M.; Ciopec, M.; Negrea, A.; Grad, O.; Ianăși, C.; Ivankov, O.; Milanović, M.; Stijepović, I.; Almásy, L. Comparison of Structure and Adsorption Properties of Mesoporous Silica Functionalized with Aminopropyl Groups by the Co-Condensation and the Post Grafting Methods. *Materials* **2021**, *14*, 628. [[CrossRef](#)]
21. Gervas, C.; Mubofu, E.B.; Mdoe, J.E.G.; Revaprasadu, N. Functionalized mesoporous organo-silica nanosorbents for removal of chromium (III) ions from tanneries wastewater. *J. Porous Mater.* **2016**, *23*, 83–93. [[CrossRef](#)]
22. Liu, S.; Lu, L.; Yang, Z.; Cool, P.; Vansant, E.F. Further Investigations on the Modified Stöber Method for Spherical MCM-41. *Mater. Chem. Phys.* **2006**, *97*, 203–206. [[CrossRef](#)]
23. Liu, S.; Cool, P.; Collart, O.; Van Der Voort, P.; Vansant, E.F.; Lebedev, O.I.; Van Tendeloo, G.; Jiang, M. The Influence of the Alcohol Concentration on the Structural Ordering of Mesoporous Silica: Cosurfactant versus Cosolvent. *J. Phys. Chem. B* **2003**, *107*, 10405–10411. [[CrossRef](#)]



24. Ngoc Thi Le, H.; Jeong, H.K. Synthesis and Characterization of Uniform Silica Nanoparticles on Nickel Substrate by Spin Coating and Sol–Gel Method. *Chem. Phys. Lett.* **2014**, *592*, 349–354. [[CrossRef](#)]
25. El-Safty, S.A. Instant Synthesis of Mesoporous Monolithic Materials with Controllable Geometry, Dimension and Stability: A Review. *J. Porous Mater.* **2011**, *18*, 259–287. [[CrossRef](#)]
26. Courtois, J.; Byström, E.; Irgum, K. Novel Monolithic Materials Using Poly(Ethylene Glycol) as Porogen for Protein Separation. *Polymer* **2006**, *47*, 2603–2611. [[CrossRef](#)]
27. Tan, S.; Wu, Q.; Wang, J.; Wang, Y.; Liu, X.; Sui, K.; Deng, X.; Wang, H.; Wu, M. Dynamic Self-Assembly Synthesis and Controlled Release as Drug Vehicles of Porous Hollow Silica Nanoparticles. *Microporous Mesoporous Mater.* **2011**, *142*, 601–608. [[CrossRef](#)]
28. Zhang, Y.B.; Qian, X.F.; Li, Z.K.; Yin, J.; Zhu, Z.K. Synthesis of Novel Mesoporous Silica Spheres with Starburst Pore Canal Structure. *J. Solid State Chem.* **2004**, *177*, 844–848. [[CrossRef](#)]
29. Pabón, E.; Retuert, J.; Quijada, R. Synthesis of Mixed Silica–Titania by the Sol–Gel Method Using Polyethylenimine: Porosity and Catalytic Properties. *J. Porous Mater.* **2007**, *14*, 151–158. [[CrossRef](#)]
30. Pirson, A.; Mohsine, A.; Marchot, P.; Michaux, B.; van Cantfort, O.; Pirard, J.P.; Lecloux, A.J. Synthesis of SiO<sub>2</sub>–TiO<sub>2</sub> Xerogels by Sol–Gel Process. *J. Sol–Gel Sci. Technol.* **1995**, *4*, 179–185. [[CrossRef](#)]
31. Dudás, Z.; Len, A.; Ianăși, C.; Paladini, G. Structural Modifications Caused by the Increasing MTES Amount in Hybrid MTES/TEOS-based Silica Xerogels. *Mater. Charact.* **2020**, *167*, 110519. [[CrossRef](#)]
32. Al-Oweini, R.; El-Rassy, H. Synthesis and Characterization by FTIR Spectroscopy of Silica Aerogels Prepared Using Several Si(OR)<sub>4</sub> and R''Si(OR')<sub>3</sub> Precursors. *J. Mol. Struct.* **2009**, *919*, 140–145. [[CrossRef](#)]
33. Brinker, C.J.; Scherer, G.W. *Sol–Gel Science: The Physics and Chemistry of Sol–Gel Processing*; Academic Press: New York, NY, USA, 1990; pp. 581–585.
34. Gallardo, J.; Galliano, P.; Durán, A. Thermal Evolution of Hybrid Sol–Gel Silica Coatings: A Structural Analysis. *J. Sol–Gel Sci. Technol.* **2000**, *19*, 393–397. [[CrossRef](#)]
35. Lenza, R.F.S.; Vasconcelos, W.L. Preparation of Silica by Sol–Gel Method Using Formamide. *Mat. Res.* **2001**, *4*, 175–179. [[CrossRef](#)]
36. Putz, A.-M.; Cecilia, S.; Ianăși, C.; Dudás, Z.; Székely, K.N.; Plocek, J.; Sfârloagă, P.; Săcărescu, L.; Almásy, L. Pore Ordering in Mesoporous Matrices Induced by Different Directing Agents. *J. Porous Mater.* **2015**, *22*, 321–331. [[CrossRef](#)]
37. Cychosz, K.A.; Thommes, M. Progress in the Physisorption Characterization of Nanoporous Gas Storage Materials. *Engineering* **2018**, *4*, 559–566. [[CrossRef](#)]
38. Thommes, M.; Kaneko, K.; Neimark, A.V.; Olivier, J.P.; Rodriguez-Reinoso, F.; Rouquerol, J.; Sing, K.S.W. Physisorption of Gases, with Special Reference to the Evaluation of Surface Area and Pore Size Distribution (IUPAC Technical Report). *Pure Appl. Chem.* **2015**, *87*, 1051–1069. [[CrossRef](#)]
39. Ahmad, A.L.; Mustafa, N.N.N. Pore Surface Fractal Analysis of Palladium–Alumina Ceramic Membrane Using Frenkel–Halsey–Hill (FHH) Model. *J. Colloid Interface Sci.* **2006**, *301*, 575–584. [[CrossRef](#)]
40. Lelong, G.; Bhattacharyya, S.; Kline, S.; Cacciaguerra, T.; Gonzalez, M.A.; Saboungi, M.-L. Effect of Surfactant Concentration on the Morphology and Texture of MCM-41 Materials. *J. Phys. Chem. C* **2008**, *112*, 10674–10680. [[CrossRef](#)]
41. Soper, A.K. Radical Re-Appraisal of Water Structure in Hydrophilic Confinement. *Chem. Phys. Lett.* **2013**, *590*, 1–15. [[CrossRef](#)]
42. Goworek, J.; Kierys, A.; Gac, W.; Borówka, A.; Kusak, R. Thermal Degradation of CTAB in As-Synthesized MCM-41. *J. Therm. Anal. Calorim.* **2009**, *96*, 375–382. [[CrossRef](#)]
43. Foo, K.Y.; Hameed, B.H. Insights into the Modeling of Adsorption Isotherm Systems. *Chem. Eng. J.* **2010**, *156*, 2–10. [[CrossRef](#)]
44. Alberti, G.; Amendola, V.; Pesavento, M.; Biesuz, R. Beyond the Synthesis of Novel Solid Phases: Review on Modelling of Sorption Phenomena. *Coord. Chem. Rev.* **2012**, *256*, 28–45. [[CrossRef](#)]
45. Langmuir, I. The Adsorption of Gases on Plane Surfaces of Glass, Mica and Platinum. *J. Am. Chem. Soc.* **1918**, *40*, 1361–1403. [[CrossRef](#)]
46. Freundlich, H. Über die Adsorption in Lösungen. *Z. Phys. Chem.* **1906**, *57*, 385–470. [[CrossRef](#)]
47. Sips, R. On the Structure of a Catalyst Surface. *J. Chem. Phys.* **1948**, *16*, 490–495. [[CrossRef](#)]
48. Ciopec, M.; Davidescu, C.; Negrea, A.; Lupa, L.; Negrea, P.; Popa, A.; Muntean, C. Use of D2EHPA impregnated XAD7 resin for the removal of Cd(II) and Zn(II) from aqueous solutions. *Environ. Eng. Manag. J.* **2011**, *10*, 1597–1608. [[CrossRef](#)]
49. Anirudhan, T.S.; Senan, P.; Suchithra, P.S. Evaluation of Iron(III)-Coordinated Amino-Functionalized Poly(Glycidyl Methacrylate)-Grafted Cellulose for Arsenic(V) Adsorption from Aqueous Solutions. *Water Air Soil Pollut.* **2011**, *220*, 101–116. [[CrossRef](#)]
50. Mishra, P.C.; Patel, R.K. Removal of Lead and Zinc Ions from Water by Low Cost Adsorbents. *J. Hazard. Mater.* **2009**, *168*, 319–325. [[CrossRef](#)]
51. Keochaiyom, B.; Wan, J.; Zeng, G.; Huang, D.; Xue, W.; Hu, L.; Huang, C.; Zhang, C.; Cheng, M. Synthesis and Application of Magnetic Chlorapatite Nanoparticles for Zinc (II), Cadmium (II) and Lead (II) Removal from Water Solutions. *J. Colloid Interface Sci.* **2017**, *505*, 824–835. [[CrossRef](#)]
52. Nguyen, T.C.; Loganathan, P.; Nguyen, T.V.; Vigneswaran, S.; Kandasamy, J.; Naidu, R. Simultaneous Adsorption of Cd, Cr, Cu, Pb, and Zn by an Iron-Coated Australian Zeolite in Batch and Fixed-Bed Column Studies. *Chem. Eng. J.* **2015**, *270*, 393–404. [[CrossRef](#)]
53. Hubert, B.; Setiawan, Y.; Soetaredjo, F.E.; Hartono, S.B. Adsorption of Pb on Thiol Modified Magnetic Mesoporous Silica. *ARPN J. Eng. Appl. Sci.* **2018**, *13*, 859–863.

54. Fan, H.; Ma, X.; Zhou, S.; Huang, J.; Liu, Y.; Liu, Y. Highly Efficient Removal of Heavy Metal Ions by Carboxymethyl Cellulose-Immobilized Fe<sub>3</sub>O<sub>4</sub> Nanoparticles Prepared via High-Gravity Technology. *Carbohydr. Polym.* **2019**, *213*, 39–49. [[CrossRef](#)] [[PubMed](#)]
55. Tian, Q.; Wang, X.; Mao, F.; Guo, X. Absorption Performance of DMSA Modified Fe<sub>3</sub>O<sub>4</sub>@SiO<sub>2</sub> Core/Shell Magnetic Nanocomposite for Pb<sup>2+</sup> Removal. *J. Cent. South Univ.* **2018**, *25*, 709–718. [[CrossRef](#)]
56. Ahmad, N.; Sereshti, H.; Mousazadeh, M.; Rashidi Nodeh, H.; Kamboh, M.A.; Mohamad, S. New Magnetic Silica-Based Hybrid Organic-Inorganic Nanocomposite for the Removal of Lead(II) and Nickel(II) Ions from Aqueous Solutions. *Mater. Chem. Phys.* **2019**, *226*, 73–81. [[CrossRef](#)]
57. Wang, J.; Zheng, S.; Shao, Y.; Liu, J.; Xu, Z.; Zhu, D. Amino-Functionalized Fe<sub>3</sub>O<sub>4</sub>@SiO<sub>2</sub> Core-Shell Magnetic Nanomaterial as a Novel Adsorbent for Aqueous Heavy Metals Removal. *J. Colloid Interface Sci.* **2010**, *349*, 293–299. [[CrossRef](#)]
58. Dursun, A.Y. A Comparative Study on Determination of the Equilibrium, Kinetic and Thermodynamic Parameters of Biosorption of Copper(II) and Lead(II) Ions onto Pretreated *Aspergillus niger*. *Biochem. Eng. J.* **2006**, *28*, 187–195. [[CrossRef](#)]
59. Rajput, S.; Singh, L.P.; Pittman, C.U.; Mohan, D. Lead (Pb<sup>2+</sup>) and Copper (Cu<sup>2+</sup>) Remediation from Water Using Superparamagnetic Maghemite (γ-Fe<sub>2</sub>O<sub>3</sub>) Nanoparticles Synthesized by Flame Spray Pyrolysis (FSP). *J. Colloid Interface Sci.* **2017**, *492*, 176–190. [[CrossRef](#)]
60. Giraldo, L.; Erto, A.; Moreno-Piraján, J.C. Magnetite Nanoparticles for Removal of Heavy Metals from Aqueous Solutions: Synthesis and Characterization. *Adsorption* **2013**, *19*, 465–474. [[CrossRef](#)]
61. Mahdavi, S.; Jalali, M.; Afkhami, A. Heavy Metals Removal from Aqueous Solutions Using TiO<sub>2</sub>, MgO, and Al<sub>2</sub>O<sub>3</sub> Nanoparticles. *Chem. Eng. Commun.* **2013**, *200*, 448–470. [[CrossRef](#)]
62. Hadi Najafabadi, H.; Irani, M.; Roshanfekar Rad, L.; Heydari Haratameh, A.; Haririan, I. Removal of Cu<sup>2+</sup>, Pb<sup>2+</sup> and Cr<sup>6+</sup> from Aqueous Solutions Using a Chitosan/Graphene Oxide Composite Nanofibrous Adsorbent. *RSC Adv.* **2015**, *5*, 16532–16539. [[CrossRef](#)]
63. Tighadouini, S.; Radi, S.; Bacquet, M.; Degoutin, S.; Zaghrioui, M.; Jodeh, S.; Warad, I. Removal Efficiency of Pb(II), Zn(II), Cd(II) and Cu(II) from Aqueous Solution and Natural Water by Ketoenol–Pyrazole Receptor Functionalized Silica Hybrid Adsorbent. *Sep. Sci. Technol.* **2017**, *52*, 608–621. [[CrossRef](#)]
64. Raji, F.; Saraeian, A.; Pakizeh, M.; Attarzadeh, F. Removal of Pb(II) from Aqueous Solution by Mesoporous Silica MCM-41 Modified by ZnCl<sub>2</sub>: Kinetics, Thermodynamics, and Isotherms. *RSC Adv.* **2015**, *5*, 37066–37077. [[CrossRef](#)]
65. Huang, J.; Ye, M.; Qu, Y.; Chu, L.; Chen, R.; He, Q.; Xu, D. Pb (II) Removal from Aqueous Media by EDTA-Modified Mesoporous Silica SBA-15. *J. Colloid Interface Sci.* **2012**, *385*, 137–146. [[CrossRef](#)] [[PubMed](#)]
66. Unob, F.; Wongsiri, B.; Phaeon, N.; Puanngam, M.; Shiowatana, J. Reuse of Waste Silica as Adsorbent for Metal Removal by Iron Oxide Modification. *J. Hazard. Mater.* **2007**, *142*, 455–462. [[CrossRef](#)]
67. Nicola, R.; Costişor, O.; Ciopec, M.; Negrea, A.; Lazău, R.; Ianăşi, C.; Picioruş, E.-M.; Len, A.; Almásy, L.; Szerb, E.I.; et al. Silica-Coated Magnetic Nanocomposites for Pb<sup>2+</sup> Removal from Aqueous Solution. *Appl. Sci.* **2020**, *10*, 2726. [[CrossRef](#)]
68. Qureashi, A.; Pandith, A.H.; Bashir, A.; Manzoor, T.; Malik, L.A.; Sheikh, F.A. Citrate Coated Magnetite: A Complete Magneto Dielectric, Electrochemical and DFT Study for Detection and Removal of Heavy Metal Ions. *Surf. Interfaces* **2021**, *23*, 101004. [[CrossRef](#)]
69. Melnyk, I.V.; Pogorilyi, R.P.; Zub, Y.L.; Vaclavikova, M.; Gdula, K.; Dąbrowski, A.; Seisenbaeva, G.A.; Kessler, V.G. Protection of Thiol Groups on the Surface of Magnetic Adsorbents and Their Application for Wastewater Treatment. *Sci. Rep.* **2018**, *8*, 8592. [[CrossRef](#)]
70. Zhang, X.; Cheng, T.; Chen, C.; Wang, L.; Deng, Q.; Chen, G.; Ye, C. Synthesis of a Novel Magnetic Nano-Zeolite and Its Application as an Efficient Heavy Metal Adsorbent. *Mater. Res. Express* **2020**, *7*, 085007. [[CrossRef](#)]
71. Kaliannan, D.; Palaninaicker, S.; Palanivel, V.; Mahadeo, M.A.; Ravindra, B.N.; Jae-Jin, S. A Novel Approach to Preparation of Nano-Adsorbent from Agricultural Wastes (*Saccharum Officinarum* Leaves) and Its Environmental Application. *Environ. Sci. Pollut. Res.* **2019**, *26*, 5305–5314. [[CrossRef](#)]
72. Yang, P.; Li, F.; Wang, B.; Niu, Y.; Wei, J.; Yu, Q. In Situ Synthesis of Carbon Nanotube-Steel Slag Composite for Pb(II) and Cu(II) Removal from Aqueous Solution. *Nanomaterials* **2022**, *12*, 1199. [[CrossRef](#)] [[PubMed](#)]
73. Kotsyuda, S.S.; Tomina, V.V.; Zub, Y.L.; Furtat, I.M.; Lebed, A.P.; Vaclavikova, M.; Melnyk, I.V. Bifunctional Silica Nanospheres with 3-Aminopropyl and Phenyl Groups. Synthesis Approach and Prospects of Their Applications. *Appl. Surf. Sci.* **2017**, *420*, 782–791. [[CrossRef](#)]
74. Mahmoud, M.E.; Fekry, N.A.; El-Latif, M.M.A. Nanocomposites of Nanosilica-Immobilized-Nanopolyaniline and Crosslinked Nanopolyaniline for Removal of Heavy Metals. *Chem. Eng. J.* **2016**, *304*, 679–691. [[CrossRef](#)]
75. Ramkumar, J.; Majeed, J.; Chandramouleeswaran, S. Insight to Sorption Mechanism Employing Nanocomposite: Case Study of Toxic Species Removal. *Microporous Mesoporous Mater.* **2021**, *314*, 110858. [[CrossRef](#)]
76. De, S.; Malik, S.; Ghosh, A.; Saha, R.; Saha, B. A review on natural surfactants. *RSC Adv.* **2015**, *5*, 65757. [[CrossRef](#)]
77. Putz, A.-M.; Wang, K.; Len, A.; Plocek, J.; Bezdicka, P.; Kopitsa, G.P.; Khamova, T.V.; Ianăşi, C.; Săcărescu, L.; Mitróová, Z.; et al. Mesoporous Silica Obtained with Methyltriethoxysilane as Co-Precursor in Alkaline Medium. *Appl. Surf. Sci.* **2017**, *424*, 275–281. [[CrossRef](#)]

78. Kuklin, A.I.; Soloviov, D.V.; Rogachev, A.V.; Utrobin, P.K.; Kovalev, Y.S.; Balasoiu, M.; Ivankov, O.I.; Sirotin, A.P.; Murugova, T.N.; Petukhova, T.B.; et al. New Opportunities Provided by Modernized Small-Angle Neutron Scattering Two-Detector System Instrument (YuMO). *J. Phys. Conf. Ser.* **2011**, *291*, 12013. [[CrossRef](#)]
79. Kuklin, A.I.; Rogov, A.D.; Gorshkova, Y.E.; Utrobin, P.K.; Kovalev, Y.S.; Rogachev, A.V.; Ivankov, O.I.; Kutuzov, S.A.; Soloviov, D.V.; Gordeliy, V.I. Analysis of Neutron Spectra and Fluxes Obtained with Cold and Thermal Moderators at IBR-2 Reactor: Experimental and Computer-Modeling Studies. *Phys. Part. Nucl. Lett.* **2011**, *8*, 119. [[CrossRef](#)]
80. Kuklin, A.I.; Islamov, A.K.; Gordeliy, V.I. Scientific Reviews: Two-Detector System for Small-Angle Neutron Scattering Instrument. *Neutron News* **2005**, *16*, 16–18. [[CrossRef](#)]
81. Soloviev, A.G.; Solovjeva, T.M.; Ivankov, O.I.; Soloviov, D.V.; Rogachev, A.V.; Kuklin, A.I. SAS program for two-detector system: Seamless curve from both detectors. *J. Phys. Conf. Ser.* **2017**, *848*, 012020. [[CrossRef](#)]
82. Strunz, P.; Saroun, J.; Mikula, P.; Lukas, P.; Eichhorn, F. Double-Bent-Crystal Small-Angle Neutron Scattering Setting and its Applications. *J. Appl. Cryst.* **1997**, *30*, 844–848. [[CrossRef](#)]